Particuology 115 (2026) 321–335

Contents lists available at ScienceDirect

Particuology

journal homepage: www.elsevier.com/locate/partic

Insights into sinkhole development in granular soils: Experimental and numerical investigations

Tung T. Hoang[a], Thanh T. Nguyen[a,*], Thien Q. Huynh[a], Thao Doan[a,b]

[a] School of Civil and Environmental Engineering, University of Technology Sydney, Ultimo, Australia
[b] Wollongong Council, Wollongong, Australia

HIGHLIGHTS

- Innovative experiment coupling model test and Particle Image Velocimetry (PIV).
- DEM simulation of sinkhole development with validation against experiment.
- Excellent agreement between experiment and DEM in four-stage development of sinkholes.
- Exploring the influence of triggering depth and compaction state on sinkhole formation.
- Interparticle evolution through transition phases of sinkhole formation.

GRAPHICAL ABSTRACT

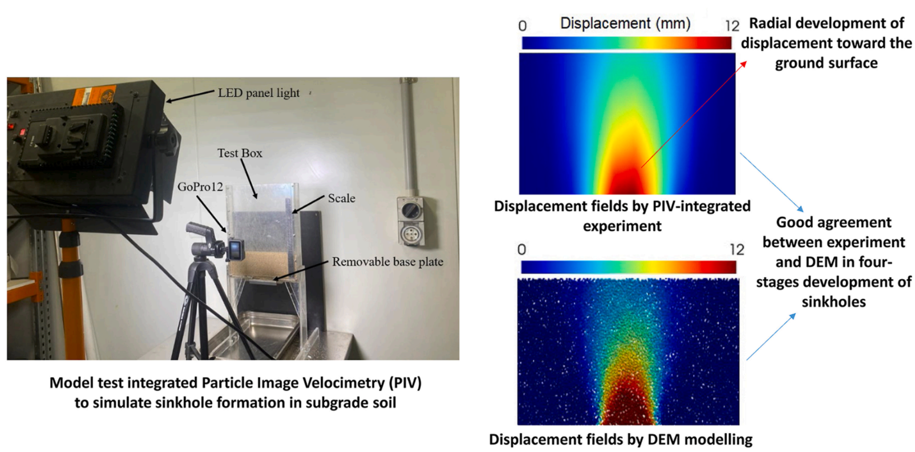

ARTICLE INFO

Keywords:
Sinkholes
Particle Image Velocimetry (PIV)
DEM
Displacement fields
Triggering depth
Compaction state

ABSTRACT

Sinkholes, a common geotechnical failure, have been reported more frequently in recent years due to complex climate change and urbanisation. This study investigates mechanisms of sinkhole development, considering the influence of triggering depth and compaction degree through experiments integrated with Particle Image Velocimetry (PIV) technique and Discrete Element Method (DEM). Laboratory tests simulating the formation of sinkhole in subgrade soil are carried out under varying triggering depths and void ratios, where the soil displacement is recorded over time. DEM simulations are performed and validated against the experimental results analysed by PIV technique. The results show good agreement between DEM and experimental investigations, especially in capturing time-dependent stages and displacement fields of sinkhole development. Furthermore, the numerical investigation indicates that increasing the triggering depth results in later development of sinkhole with greater vertical displacement around the triggering point to promote its propagation towards the ground surface. Interestingly, dense soil exhibits highly localised mobilisation confined within well-defined displacement boundaries, whereas loose soil displays a wider displacement zone characterised by a

* Corresponding author.
E-mail address: thanh.nguyen-4@uts.edu.au (T.T. Nguyen).

https://doi.org/10.1016/j.partic.2026.06.006
Received 21 March 2026; Received in revised form 19 May 2026; Accepted 4 June 2026
Available online 12 June 2026

funnel-shaped pattern. The interparticle contact behaviour further releases the insightful mechanism of sinkhole progression, giving considerable value to our understanding and prediction of this catastrophic failure.

1. Introduction

Sinkholes resulting from the collapse of surface soil layers, triggered by either human activities or natural processes, have become a serious geohazard worldwide (Dave & Juneja, 2023; Kaufmann, 2007; Thornbush, 2017). Of these, anthropogenic drivers have been identified as the dominant trigger and often lead to more severe consequences, particularly in urban areas where buried infrastructure and groundwater disturbances are common (Ghaayeshthree & Mohd Arif Bin, 2025; Youssef et al., 2016). The collapse process generally initiates with the presence of a small subsurface void which progressively expands over time and ultimately causes sudden ground surface collapse with limited or no prior warning (Panjami & Anbazhagan, 2025). When sinkholes occur beneath roads, buildings, or other critical assets, they can result in substantial structural damage, disruption to essential services and significant economic loss. For example, in the US, sinkhole-related damage has been reported at approximately USD 300 million annually, with cumulative losses reaching USD 1.4 billion in Florida between 2006 and 2010 (Muili & Babaie, 2025). In Australia, the Lane Cove Tunnel sinkhole resulted in consequential damage and economic losses totalling approximately AUD 21 million in 2005 (Burman et al., 2018). Beyond economic impacts, sinkholes pose serious risks to public safety (Coşkuner et al., 2025; Gutiérrez et al., 2015; Waltham, 2008). For instance, in Italy, sinkhole events have been reported in a national sinkhole catalogue to have caused 146 deaths, 94 injuries (Vennari & Parise, 2022). As a result, considerable number of studies have been devoted to deepening the understanding of sinkhole hazards, including formation mechanisms (Doğan & Yılmaz, 2011; Jiang et al., 2017; Zhao et al., 2021) and their geometrical and developmental characteristics (Eren et al., 2024; Kobal et al., 2015).

During the initial development process of sinkhole, the soil mass above the cavity can temporarily rearrange to form a self-supporting arch that transfers load to the surrounding ground. This phenomenon, known as soil arching, has been widely studied in geotechnical engineering applications such as underground tunnels (Chai et al., 2018; He et al., 2023; Lin et al., 2019), pile and soil-cement column embankments (Al-Naddaf et al., 2019; Nguyen, Nguyen, et al., 2022) and retaining walls (Fan et al., 2023; Qiu & Grabe, 2012; Tangjarusritaratorn et al., 2022). Numerous experimental and analytical studies have also been carried out to investigate a number of governing factors contributing to the sinkhole development, including: (i) the thickness of overburden soil, which controls cavity propagation and surface expression in trapdoor/centrifuge-type physical modelling (Xu et al., 2019); (ii) soil state variables (e.g., density, strength and backfill compaction), which influence arching stability, soil movement localisation, and failure pattern (Ferentinou, 2020; Jacobsz, 2015); (iii) grading and particle-size distribution, which strongly govern susceptibility to particle migration and void growth, particularly for sinkholes associated with defective buried pipes (Indiketiya et al., 2019); and (iv) subsurface disturbance which can be analytically measured to estimate mobilisation and collapse likelihood following underground voiding (Whittaker & Reddish, 1989). Although prior experimental studies have characterised sinkhole evolution mainly through macroscopic responses (i.e., surface settlement patterns, cavity growth, and collapse geometry), the fundamental grain-scale mechanisms and stress-transfer processes driving these observations remain insufficiently understood.

Numerical methods such as the Discrete Element Method (DEM) have recently become reliable tools for investigating the sinkhole progression mechanism, enabling the temporal and spatial tracking of soil particle motion and contact forces and examining the micro-macro relationships governing sinkhole development (Szmigiel & Tajduś, 2025, pp. 293–312). DEM has been widely applied to study the soil arching during void growth (Deng et al., 2025; Elabd et al., 2025; Han et al., 2012; Zhou et al., 2023). For instance, cavity stability and ground collapse process were examined through DEM simulations, offering a benchmark against analytical and Boundary Element Method methods, highlighting the interaction of material strength and the material removal (Al-Halbouni et al., 2020). Moreover, DEM has also been coupled with computational fluid dynamics (CFD) to represent multiphase processes where seepage and particle displacement contribute to void growth and collapse (Duan et al., 2023; Ibrahim & Meguid, 2023; Wang et al., 2025). Although these abovementioned studies provided valuable insights into the multifaceted processes governing sinkhole, they often lack robust validation against physical experiments and field observations - for instance, a DEM analysis of geogrid-reinforced embankments over voids was validated only against prior experiments (Feng & Wang, 2025) or a 2D DEM sinkhole simulation relied primarily on numerical benchmarks rather than comprehensive physical test (Al-Halbouni et al., 2018). Additionally, only a limited number of studies has examined the coupled effects of triggering depth D_t (depth of the initial cavity or defect, see Fig. 1) and compaction state (porosity or void ratio) on soil displacement. Moreover, the influence of particle-size scaling on soil mobilisation remained underexplored, leaving a gap in assessing DEM model reliability in capturing sinkhole propagation.

The objective of this study is therefore to investigate the sinkhole formation mechanisms using an innovative framework coupling PIV-integrated experiment and DEM modelling. Laboratory tests mimicking sinkhole development are carried out and the recorded results are analysed by PIV technique to capture displacement fields. The experiment is then simulated by DEM with the results that are compared with each other, showing their good agreement in presenting the four-stage development of sinkhole. The effects of varying triggering depths and compaction degrees, which control the stress state and mobilisation behaviour of subsurface soil are systematically examined, clarifying how these factors influence the collapse of surface soil. Beyond macroscopic observation, grain-scale analysis of particle contacts, force chains and arching evolution are also discussed in detail to reveal the interparticle mechanisms governing bulk soil behaviour during sinkhole development. This study enhances our understanding of the progression of sinkhole and its governing factors through combined experimental-numerical investigations, giving considerable value to prediction and measure of sinkhole development in practice.

2. Theoretical background

2.1. Sinkhole formation mechanism

Sinkholes occur when overlying soil mass can no longer support itself due to the formation and progressive enlargement of subsurface cavities (Augarde et al., 2003). Fig. 1 shows a conceptual four-stage mechanism of sinkhole formation under a road, where an initial small void or cavity at depth D_t (i.e., triggering depth) from the subsoil surface is illustrated as an example among common factors inducing sinkholes. Such a void may form and expand due to water table fluctuations, leaking pipelines, dissolution of soluble bedrock and chemical reactions in soil (Kaufmann, 2014; Xiao et al., 2020; Yumba et al., 2024). The formation of an initial cavity is accompanied by the loss of overlying soil, resulting in a temporary soil arch above the cavity (see Fig. 1a). With ongoing soil loss, the cavity expands over time (see Fig. 1b). When the subsurface cavity grows to a certain size, the overlying soil layer becomes weaker and cracks on the road layer appear (Fig. 1c). Finally, a sudden collapse occurs as the soil fails into the enlarged cavity and damages the surface infrastructure (Fig. 1d). Notably, this collapse can be abrupt and unpredictable, often resulting in severe consequences.

2.2. Soil displacement captured by Particle Image Velocimetry (PIV) technique

In this study, Particle Image Velocimetry (PIV) was used to analyse sinkhole progression in the experiment, so its background and algorithm are briefly introduced in this section. This technique was originally developed for fluid mechanics experiments by Adrian (1991). Over time, researchers have modified and adopted this method for soil movement and deformation tracking. In this study, a MATLAB integrated image analysis module, GeoPIV-RG by Stanier et al. (2015) was ultilised. This module integrates the reliability guided (RG) computation method to analyse soil texture movements from high-resolution images captured by camera (Stanier et al., 2015). Firstly, input information including the region of interest (RoI), the analysis mesh and key processing parameters (e.g., subset size, spacing, correlation thresholds …) are determined. A seed subset is then selected within the predefined RoI in the reference image (image 1) and a corresponding target image (image 2) is defined. After that, normalised cross correlation (NCC) method is performed to calculate the seed subset displacement to the nearest integer pixel. The seed match is accepted when the zero-normalised cross-correlation coefficient (i.e., CC_{ZNCC}), exceeds a user-defined threshold $CC_{ZNCC\_seed\_tol}$. The CC_{ZNCC} value indicates the degree of match between reference and target subset, where three distinct values 1, 0 and −1 correspond to perfect, zero and inverse correlation, respectively (Pan et al., 2010). Once the seed is accepted, it provides the initial deformation guess, from which the RG computation propagates to find the displacement and deformation of all subsets across the RoI. Further details on the implementation of this technique can be found in a previous study (Pan, 2009).

Fig. 2 shows the overall working structure of this technique. A key advantage of GeoPIV-RG over conventional PIV applications is that it allows users to track larger deformation by implementing an automatic period reference image-updating scheme (Stanier et al., 2015). This helps to reduce the decorrelation and wild (erroneous) displacement vectors when particles rearrange. The CC_{ZNCC} value for a given subset in the target image, for which the RG computation has just been successfully implemented, is compared with a user-defined value, $CC_{ZNCC\_min\_tol}$, to determine whether the reference image should be updated. If that subset satisfies $CC_{ZNCC} \le CC_{ZNCC\_min\_tol}$, the reference image is updated to the target image from the last successful increment, otherwise the current reference image remains.

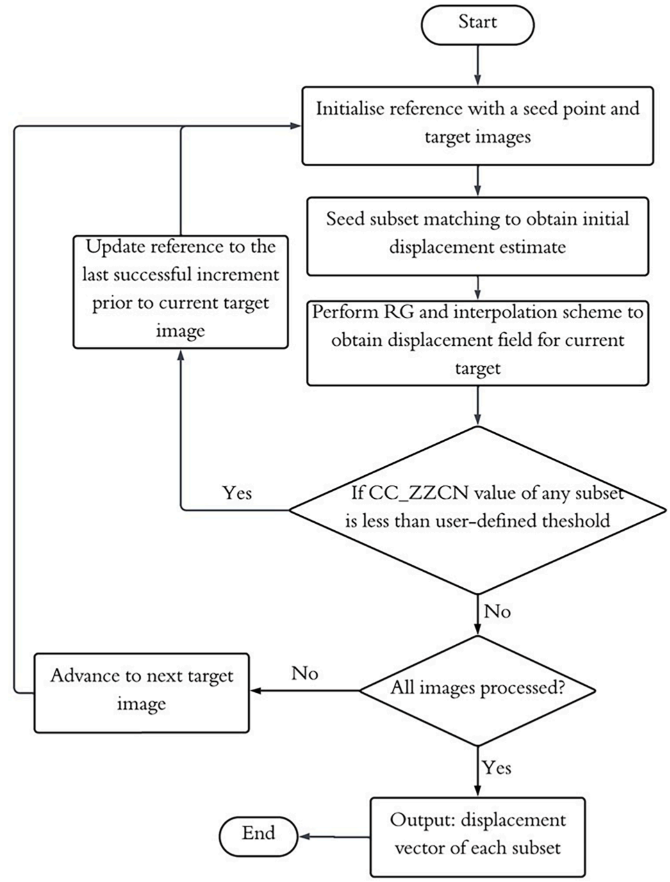

Fig. 2. GeoPIV_RG schematic workflow structure (modified from Stanier et al., 2015).

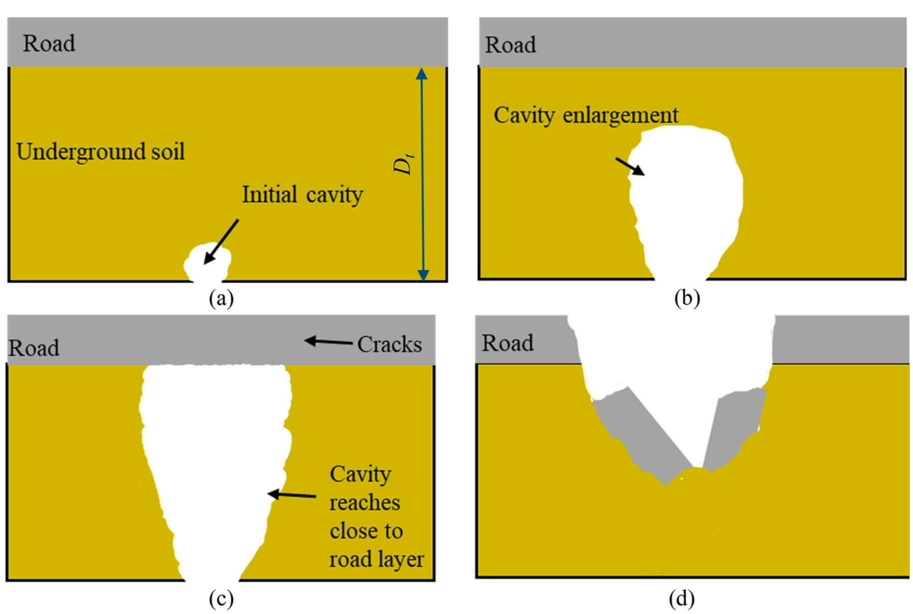

Fig. 1. Four stages of sinkhole formation under road (a) initial soil arch, (b) cavity enlargement, (c) cavity enlargement with critical damage to the ground surface and (d) complete sinkhole formation with collapse of foundation (adapted from Augarde et al., 2003).

2.3. Discrete Element Method

The Discrete Element Method (DEM) simulates granular media as an assembly of interacting particles whose motion follows Newton's laws, with interparticle forces governed by contact models. DEM provides insight into micro-to-macro behaviour, including force-chain formation and contact network evolution. As the method has been well established, its governing equations are not repeated here; details can be found in previous studies (Huynh, Nguyen, Indraratna, et al., 2025; Roessler et al., 2019). The current study adopted a non-linear Hertz-Mindlin (Hertz) model for cohesionless soil (dry sand). In this model, the normal and tangential contact forces are functions of corresponding particle overlaps and the normal and tangential contact stiffnesses. Coulomb's friction law is applied to limit the tangential force such that $|F_t| \leq \mu F_n$. This type of contact model has been widely used for granular materials in previous DEM studies (Huynh, Nguyen, Indraratna, et al., 2025), Huynh, Nguyen, Indraratna, et al., 2025) and provides an appropriate representation of the micromechanical behaviour of dry sand. The equations to compute normal force F_n and tangential force F_t are given by:

$$F_n = \left(\frac{4}{3}E^* \sqrt{R^* \delta_n}\right)\delta_n = k_n \delta_n \quad (1)$$

$$F_t = \left(8G^* \sqrt{R^* \delta_n}\right)\delta_t = k_t \delta_t \leq \mu F_n \quad (2)$$

where E^*, G^*, and R^* are the effective Young's modulus (Pa), shear modulus (Pa), and the effective radius (m), which are functions of the Young's modulus (E_1, E_2), Poisson ratios (υ_1, ν_2), and radius (R_1, R_2) of two contact particles; meanwhile δ_n, δ_t are the normal and tangential overlaps (m) between them; μ is the friction coefficient; k_n and k_t denote normal and tangential elastic stiffness (N/m), respectively.

The study employed the elastic-plastic spring-dashpot rolling model (EPSD2) (Ai et al., 2011; Iwashita & Oda, 1998) to capture the particle shape effect. A larger rolling resistance means more angular particles that the soil has. In this model, the incremental rolling torque is computed from the incremental relative rotation between two particles $\Delta\theta_r$ and the rolling stiffness k_r and is limited by a maximum value M_r^{max}, as described:

$$M_r = -k_r \Delta\theta_r, M_r \leq M_r^{max} = \mu_r R^* F_n \quad (3)$$

where M_r is the resistive torque (N·m); μ_r represents the rolling friction coefficient.

3. Experimental investigations

3.1. Material and calibration test on interparticle friction parameters

In this study, dry sand was used in the experiment, including calibration test to determine friction coefficients for particles in DEM modelling and laboratory test of sinkhole formation. Although soil under transport infrastructure can vary widely from clays to sands that might affect how soil particles clump and migrate in specific regions, the major stages of sinkhole development and collapse are often found identical (Park et al., 2024; Yumba et al., 2024). To ensure the 4 major stages of sinkhole development (Fig. 1) to be captured clearly through the PIV technique, this study employed uniform sand (i.e., 0.6-1.0 mm). This material provides more stable flow behaviour compared to cohesive soils (Huynh, Nguyen, & Indraratna, 2025) that facilitated image-based analysis and numerical modelling, thereby promoting accurate and insightful understanding.

A simple lifting cylinder (LC) test was firstly carried out to calibrate the microscopic parameters of the dry sand for DEM simulations, particularly the sliding and rolling friction coefficients as they are the dominant factors governing the macro response for non-cohesive soils (Doan et al., 2023; Roessler et al., 2019; Zhang et al., 2023). The test provides the angle of repose (AoR) formed by free flow of the material under gravity, which is used as the calibration target. The calibration of sliding and rolling friction coefficients using this method is considered appropriate in the current numerical investigations. This is because sinkhole development and collapse are primarily governed by particle loss and the free flow of granular materials under limited lateral confinement. For example, one of the most common scenarios of sinkhole is at shallow layer, i.e., 1-2m under roads and railways where confinement is often small or even negligible (Nguyen & Indraratna, 2023). Further, when being triggered by an initial cavity (Fig. 1), soil collapse occurs at internal side of the cavity due to low or zero confinement. In this context, the angle of repose test became relevant as it can reproduce the free flow and bulk frictional behaviour of particles. The experimental configuration employed a hollow cylindrical container (internal diameter = 100 mm) filled with the dry sand to a depth of 100 mm. Following gravitational settling, the container was withdrawn upward at a controlled rate of 8 mm/s, allowing the material to discharge under quasi-static flow while suppressing particle splashing (Roessler et al., 2019). As the cylinder was withdrawn, the granular assembly was released from lateral confinement, allowing the particles to spread outward under gravity. This unrestrained motion led to the development of a stable conical pile, from which the angle of repose of the bulk material was determined as Fig. 3. The measured angle of

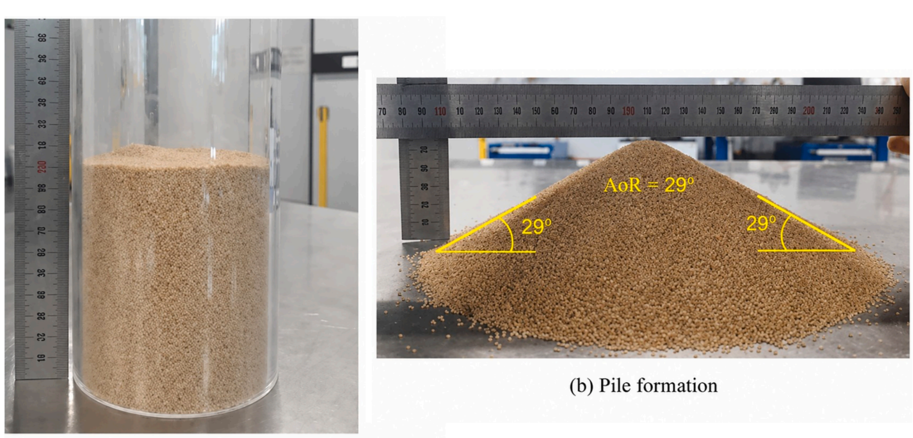

(a) Filling stage
(b) Pile formation

Fig. 3. Lifting cylinder test: (a) filling stage and (b) pile formation.

repose (AoR) was approximately 29°, which was used to compare with DEM simulation results in order to determine the appropriate sliding and rolling friction coefficients.

Fig. 4(a) illustrates how the angle of repose (AoR) responds to changes in the sliding friction coefficient (μ_s) with the rolling friction coefficient set at $\mu_r = 0.0$. The results indicate that the AoR increases with increasing μ_s. The experimentally measured angle of repose was 17.5°, and a sliding friction coefficient of $\mu_s = 0.4$ was adopted because it provided the closest agreement with the experimental measurement. This value was therefore adopted for the sand particles to calibrate the rolling friction coefficient. Fig. 4(b) shows the change of AoR to varying rolling friction coefficient (μ_r) with $\mu_s = 0.4$. The AoR is highly sensitive to μ_r for values below 0.5, showing a rapid increase, whereas its response becomes much less pronounced once μ_r exceeds 0.5. For instance, as μ_r increases from 0.1 to 0.5, the AoR rises markedly from 17° to 31°, while a further increase from 0.5 to 1.0 leads to a minor increase in the AoR to 33.5°. Based on these results, an appropriate μ_r of approximately 0.3 was selected, which aligns well with the experimental AoR of 29°. The DEM results show good agreement with the experimental observations, as illustrated by the AoR geometries in Fig. 4(c). The pile shapes predicted by DEM closely resemble to that obtained experimentally, and the overall pile geometries are consistent with the measured AoR. The calibrated values of $\mu_s = 0.4$ and $\mu_r = 0.3$ were therefore adopted in subsequent DEM simulations to investigate the sinkhole development mechanism.

3.2. Experimental investigation on the formation of sinkhole

3.2.1. Experimental setup and procedure

A laboratory test was set up to investigate the development of sinkhole as shown in Fig. 5. The test box consists of a transparent acrylic container (300 mm wide × 400 mm high × 50 mm thick) mounted on a sturdy support frame. A hole at the bottom of the soil domain was created by removing a plate at the bottom of the container (Fig. 5b). This hole mimics the initial defect that can be formed at a certain depth beneath roads, which then triggers sinkhole development. A GoPro 12 camera with a high resolution (i.e., 2,688 × 1520 pixels) at the frequency of 200 Hz was placed on a tripod in front of the test box to record the soil movement. An LED panel light was set behind the camera to provide uniform illumination on the front face. The camera and lighting placement were carefully set to optimise the contrast in soil colour, ensuring the high-quality images were captured. A scale was put on the front face of the box to convert displacement unit from pixel to mm.

A total of six tests were conducted to investigate sinkhole collapse through soil displacement. Three different triggering depths (D_t), 50 mm, 100 mm and 150 mm were examined under a fixed opening width ($B = 50$ mm) for loose and dense states. The dense soil specimen was prepared by compacting it in multiple layers where the mass and thickness of each layer were calculated and controlled to achieve the target values. The loose soil specimens were prepared using the same layer-by-layer mass and thickness control without compaction. This procedure ensured each layer had approximately the same void ratio (e), resulting in a uniform specimen. Void ratios (e) used in case studies are summarised in Table 1. It is noteworthy that the under-compaction process was adopted to avoid over-compaction induced by upper layers, following the well-known compaction method proposed by Ladd (1978). This method was used in past studies by our research team that can be found in past studies (Nguyen, Indraratna, & Leroueil, 2022). By varying different void ratios and soil thickness, the study clarified how soil compaction and triggering depth can affect the progress of sinkhole development.

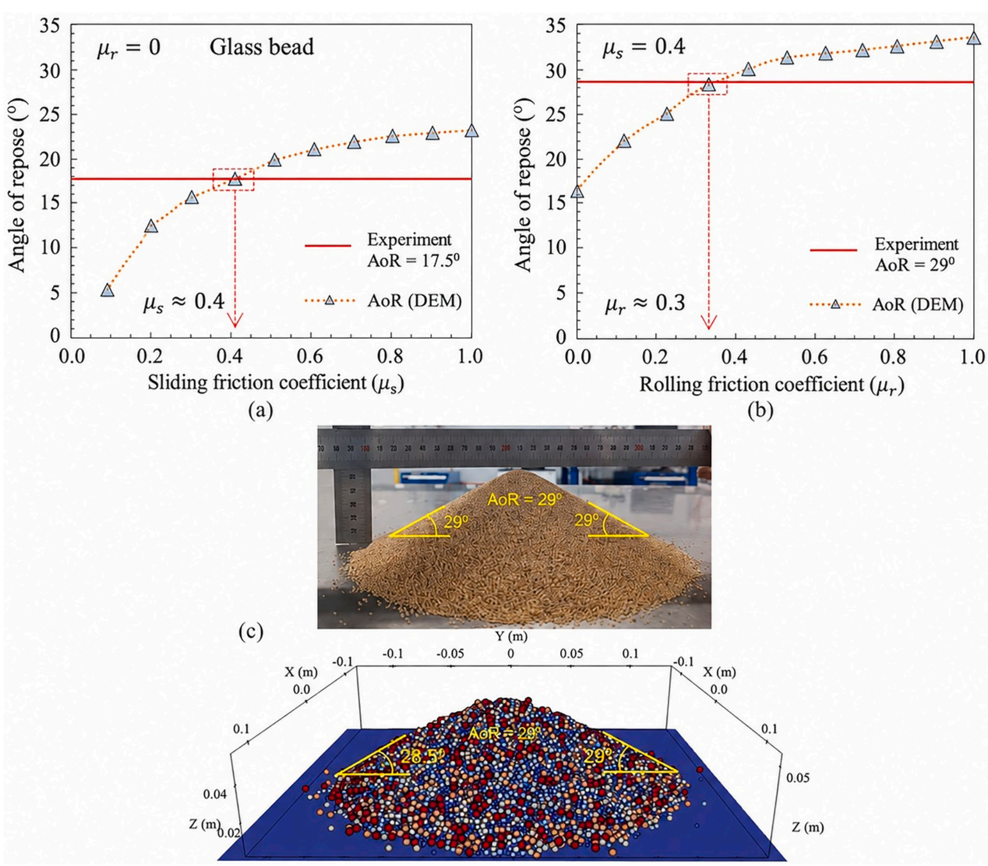

Fig. 4. Calibration results: (a) glass bead with rolling friction coefficients $\mu_r = 0.0$, (b) angular sand with sliding friction coefficients $\mu_s = 0.4$, and (c) comparison of pile shapes between DEM simulations and experiments.

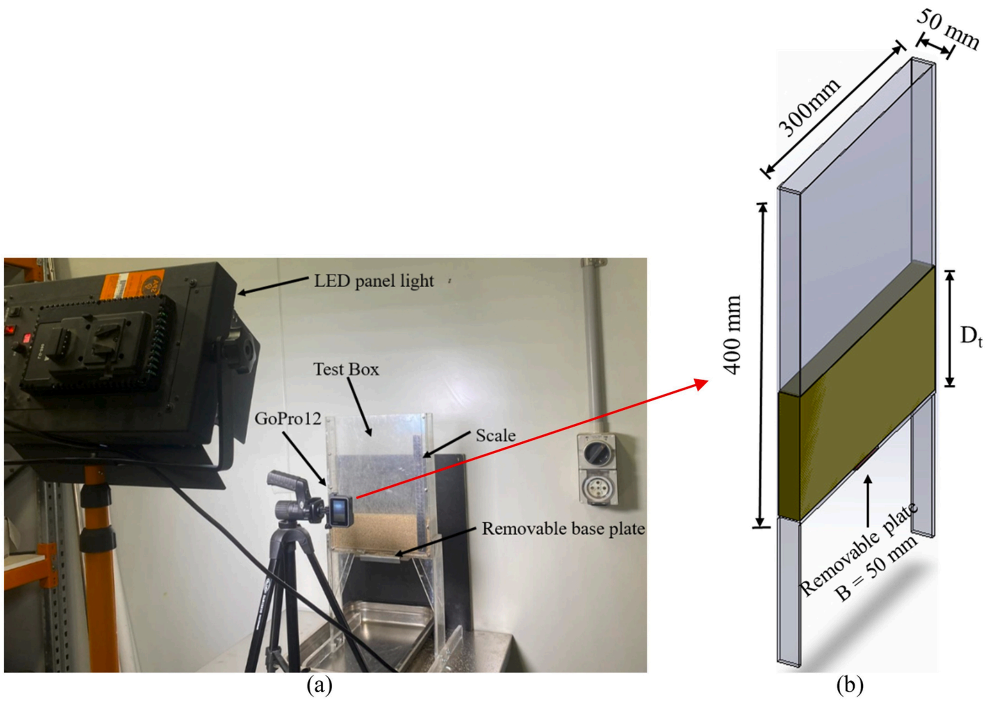

Fig. 5. Laboratory test to assess sinkhole formation: (a) Schematic of experimental setup; and (b) test box with a removal plate used to trigger sinkhole development.

Table 1
Void ratio (e) for case studies.

Depth of initial defect (triggering point) relative to gate width	e_{loose}	e_{dense}
$D_t/B = 1$	0.83	0.584
$D_t/B = 2$	0.76	0.575
$D_t/B = 3$	0.79	0.53

3.2.2. Sinkhole development captured through PIV-integrated experimental investigation

The images captured from experimental model of sinkhole development were subjected to PIV analysis techniques, with the first image taken before gate removal used as the initial reference frame. The displacement contours shown in Fig. 6 represent the cumulative movement of tracked soil-image subsets relative to their reference positions. It is also noted that a plane-strain model was adopted in this study. Although a full 3D model would better represent field-scale sinkhole development, it faces challenges in application of image-based technique which requires flat and transparent faces of the model box. Furthermore, in many cases under roads and embankments, soil often exhibits plane-strain behavior because the lateral displacement (perpendicular to the moving direction) is usually predominant over the longitudinal displacement, as commonly considered in past studies (Indraratna et al., 2021; Li et al., 2023; Wu et al., 2022). This selection does not only reflect real context (e.g., under roads and embankments) to some extent but also enables the use of PIV technique to capture the sinkhole development in greater detail. According to this figure, four major stages in the development of sinkhole can be identified. As the hole was first triggered around the bottom gate, soil begins to displace radially from the centre of the hole. In Stage 2, soil displacement continues to develop towards the ground surface, however, the surface soil particles remain static at this stage. Once the soil particles at the surface begin to displace, Stage 3 starts. The surface soil continues to displace seriously that forms large void channels connecting the surface to the trigging hole. The final stage (Stage 4) is when an open hole (sinkhole) is fully formed with slopes from the bottom hole to the ground surface. Interestingly, the largest displacement, (i.e., the centre of the displacement contours) migrates upwards as the void is fully open. The results show reasonable progress of sinkhole development in sandy soil, demonstrating success of the developed PIV-integrated experiment program. These experimental results are therefore used to validate DEM modelling presented later in this paper.

4. DEM investigation on sinkhole collapse mechanism

4.1. DEM model development

In this study, full-scale dimension of the test soil domain (i.e., 300 mm wide and 50 to 150 mm high) was developed in DEM modelling (Fig. 7), while particle sizes were scaled up 3 times to reduce computational cost. This scale-up technique was carried out with respect to past DEM investigations (Coetzee, 2019; Gao et al., 2025; Lommen et al., 2019) where the findings show that scaling particle sizes by a factor up to 4 has no significant effect on the results. The current DEM simulation used a plane-strain system, where grain behaviours in the direction perpendicular to the predominant soil behaviour domain was neglected. This method helps promote computational efficiency significantly, while maintaining intrinsic mechanical responses and failure mechanism. It is thus often adopted in numerical modelling where material behaviour occurs in a predominant plane (Fu & Dafalias, 2011; Perozzi et al., 2025). In the current test model, soil particles flowed mainly along the front view wall, i.e., from side walls surface to the triggering hole, soil behaviour outside of this plane can thus be neglected. For all cases of DEM modelling, the dimension ratio between the soil height (identical to the triggering depth D_t shown in this figure) and the largest particles (3 mm) varied from 16.7 to 52, which were large enough to neglect boundary and scale effects in the plane-strain view. The dimension perpendicular to the plane view was fixed at 2.5 times the diameter of the largest particles.

Particles were then generated randomly in the DEM container and settled under gravitation. Void ratio of the numerical soil was manipulated to achieve the experimental values (refer to Table 1) by varying friction coefficients during particle settling combined with compaction. This technique is often used in DEM studies to control the initial porosity or void ratio of granular specimens (Nguyen & Indraratna, 2020). After

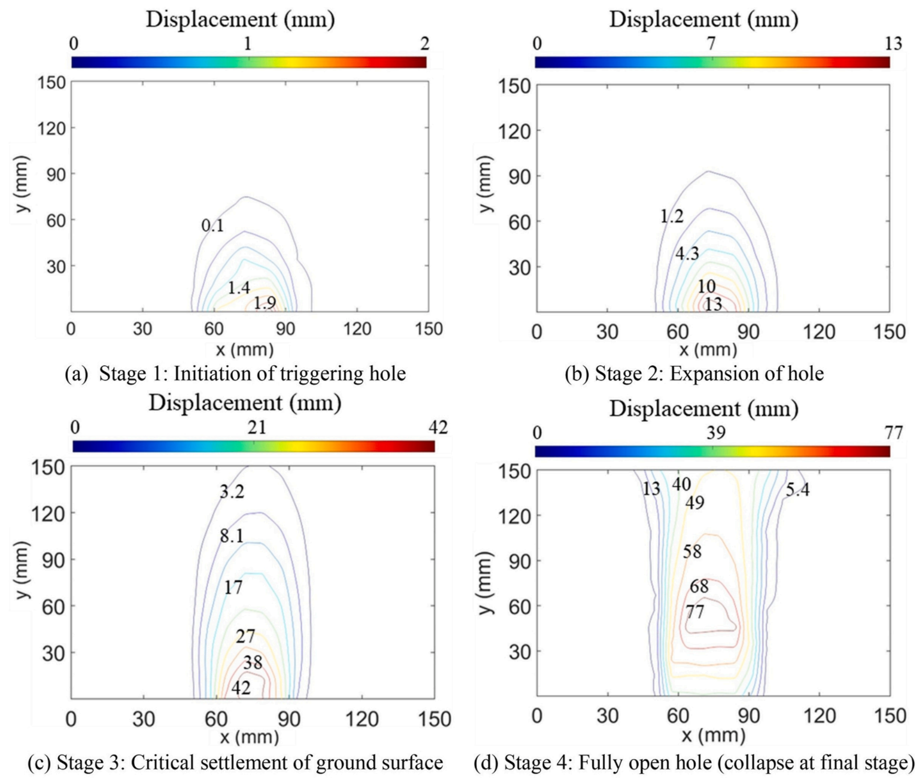

Fig. 6. Four major stages of sinkhole formation based on contour map captured from laboratory model test integrated with PIV technique: (a) Stage 1, (b) Stage 2, (c) Stage 3, (d) Stage 4.

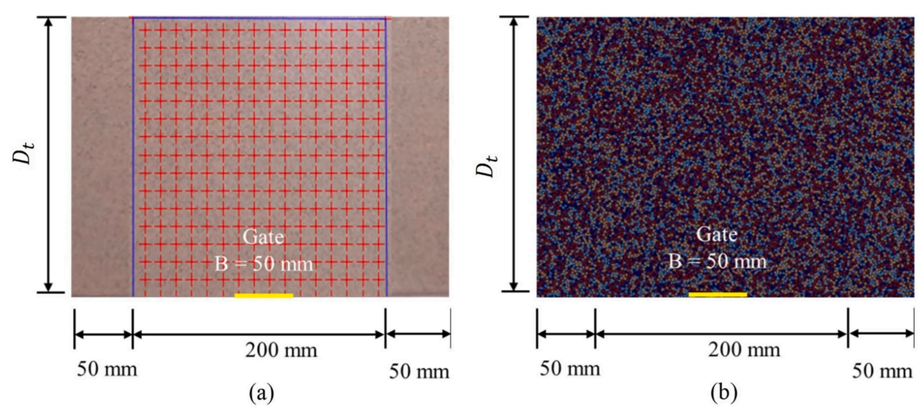

Fig. 7. (a) Experimental soil domain and region of interest for PIV; and (b) DEM domain.

achieving the desired void ration, friction coefficients were then reassigned to the calibrated values listed in Table 2 before testing execution. The DEM simulation contained approximately 18,000, 36,000 and 52,000 particles for the $D_t/B = 1$, 2 and 3 cases, respectively. It is noteworthy that the current study used spherical particles and the influence of particle shapes was considered through the rolling friction as explained in earlier sections. This approach is widely acceptable in DEM simulations when the focus is on the bulk behaviour of granular materials, such as soil displacement, flow patterns, and the contact-force evolution (Garcia Fernando et al., 2025; Huynh, Nguyen, & Indraratna, 2025; Liu et al., 2022).

Table 2
DEM input parameters.

Parameters	Values	References
Particle density (kg/m^3)	2650	Garcia Fernando et al. (2025)
Poisson's ratio	0.3	Huynh, Nguyen, and Indraratna (2025)
Young Modulus (Pa)	3×10^8	-
Particle–particle sliding friction	0.4	Calibrated result (current study)
Particle–particle rolling friction	0.3	Calibrated result (current study)
Restitution coefficient	0.2	Behjani et al. (2017)
Gravitational acceleration (m/s^2)	9.81	-

4.2. Model validation

In this section, the numerical results are compared with experimental data based on PIV analysis. Figs. 8 and 9 present the vertical displacement derived from the PIV and DEM at a critical stage for different D_t/B ratios in loose and dense states, respectively. In this analysis, a surface displacement threshold of 1.2 mm, equivalent to about 0.8% to 2.3% of

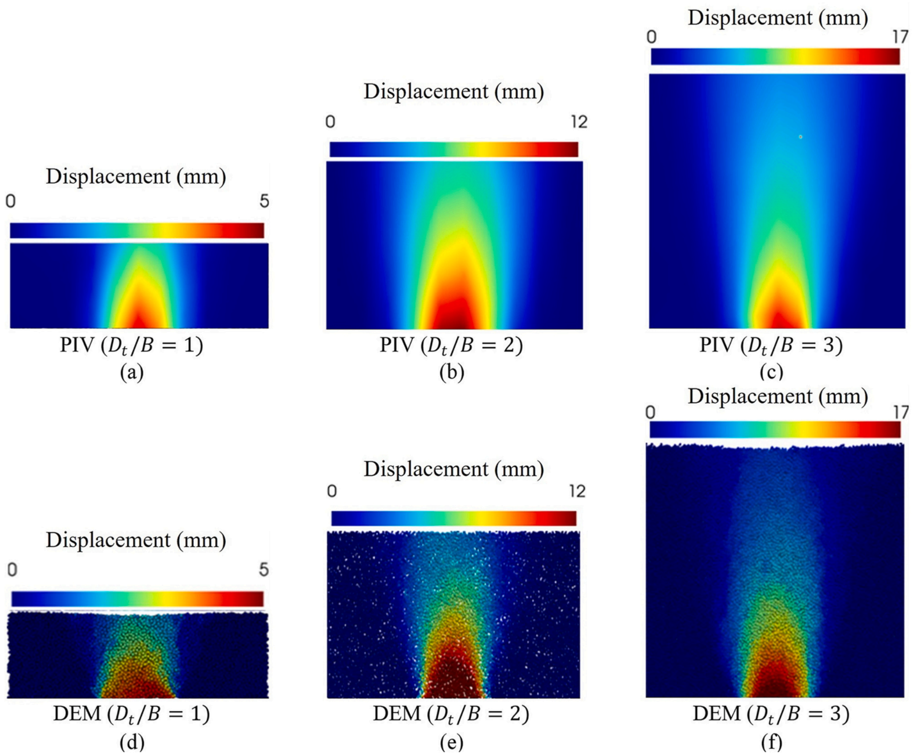

Fig. 8. Vertical displacement of loose soil at different embedment ratios obtained from PIV (a) $D_t/B = 1$, (b) $D_t/B = 2$, (c) $D_t/B = 3$ and DEM (d) $D_t/B = 1$, (e) $D_t/B = 2$ and (f) $D_t/B = 3$.

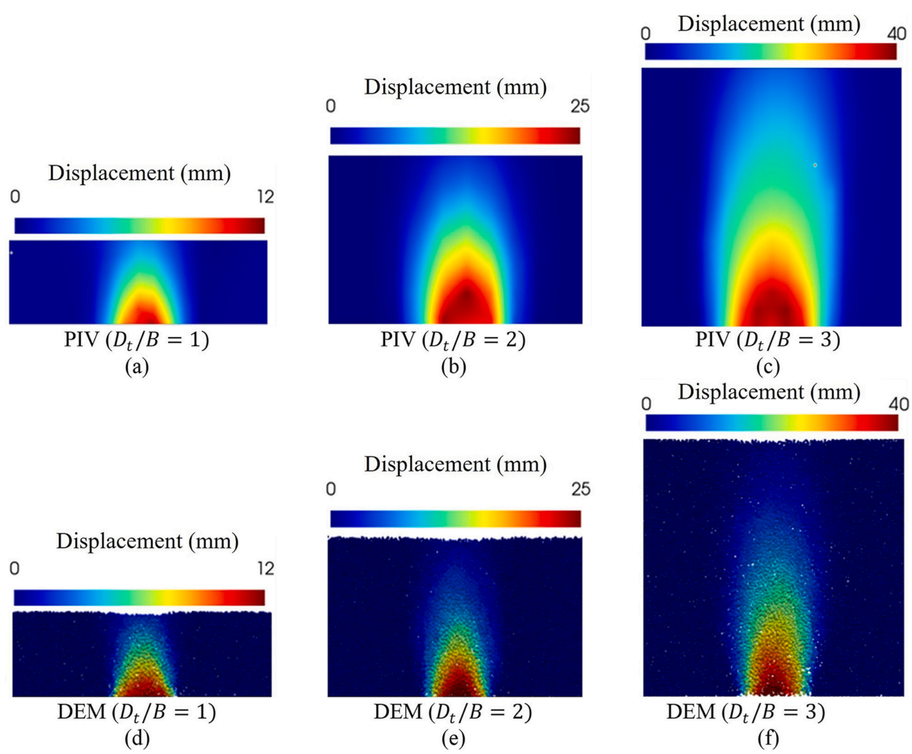

Fig. 9. Vertical displacement of dense soil at different embedment ratios obtained from PIV (a) $D_t/B = 1$, (b) $D_t/B = 2$, (c) $D_t/B = 3$ and DEM (d) $D_t/B = 1$, (e) $D_t/B = 2$ and (f) $D_t/B = 3$.

the triggering depth D_t, was considered to determine critical stage of sinkhole development. While this threshold can be small for ground settlement in roads, it can be fairly identifiable through PIV analysis, facilitating comparison among different cases. The results show a good agreement between PIV analysis and DEM simulations. For example, for $D_t/B = 3$ in dense soil, the largest degree of displacement (40 mm, dark red) was found to concentrate around the triggering hole. The magnitude of displacement decreases gradually when closer to the soil surface, forming a full development pathway of the sinkhole. The process continued by the collapse of the entire soil structure with an open hole from the initial triggering point at the bottom to the surface of the soil domain. When considering the influence of D_t, both loose and dense cases show that increasing D_t leads to an upward extension of vertical displacement region towards the ground surface and increases the displacement magnitude. For example, PIV maximum vertical displacement for the loose soil with $D_t/B = 2$ is 12 mm, while that with $D_t/B = 3$ increases by 5 mm. This outcome indicates that a greater number of particles are involved in the mobilisation process when D_t/B ratio increases from 1 to 3.

Under different soil compaction degrees, both PIV and DEM results display notable differences in soil displacement. For the dense case, deformation is highly localised, forming well-defined failure surfaces. In contrast, the loose cases show diffuse displacement, spreading over a wider region. For instance, at $D_t/B = 3$, the experimental results show a funnel-shaped displacement region, whereas dense soil exhibits a more parabolic profile. This difference reflects the dilative and contractive soil response for dense and loose soil, respectively, during mobilisation (Liu et al., 2024).

5. Numerical results and discussion

5.1. Influence of triggering depth and void ratio on sinkhole development

The influences of triggering depth (D_t) and void ratio on sinkhole collapse mechanism were examined through the evolution of soil displacement overlying the triggering hole. To compare different cases, the height z at which soil begins to displace clearly (i.e., reaching 1.2 mm) following gate opening was determined with time and normalised with the triggering depth, i.e., z/D_t. The value of 1.2 mm was selected because it was found to cause notable deformation of ground surface in the experiment and numerical model without a full collapse of the road foundation. Smaller or greater than this value would not provide the best observation across different cases. By using this identical threshold for different ratios D_t/B (1, 2 and 3), the impact of triggering depth D_t on the formation of sinkhole can then be evaluated. The results are then plotted against the normalised time T, i.e., t/T_c where t and T_c are the current time and the time at critical stage of sinkhole development (surface soil settles by about 1.2 mm). Using this metric, the features in soil displacement overtime under different D_t and soil states were revealed.

Fig. 10 shows how the z/D_t varies over time in loose soil. At early stages ($T \leq 0.44$), all curves remain close to $z/D_t = 0$, indicating the vertical displacements are largely confined to the cavity roof due to limited lost particles. As time progresses, the shallow condition ($D_t/B = 1$) exhibits a rapid increase in the displacement zone z/D_t, which develops from approximately 0.15 to 1.0 over a very short interval $T \approx 0.65$. This implies a sudden breakdown of the soil structure above the cavity, resulting in a rapid escalation of the sinkhole. However, when D_t/B ratio increases to 2 and 3, a more gradual development is shown. The displacement reaches 50% of z/D_t at approximately $T = 0.65$and 0.75 for $D_t/B = 2$ and 3 respectively. For $D_t/B = 3$, the displacement slowly progresses to the surface, following a linear trend. This means that increasing the depth of the triggering point (e.g., cavity or defect) would result in later and slower development of the sinkhole. For instance, in comparison to the case of $D_t/B = 1$, at $T = 1$, z/D_t increases by approximately 32% for $D_t/B = 2$ and nearly 50% for the $D_t/B = 3$.

Fig. 11 shows the evolution of z/D_t with respect to normalised time T for dense soil. The results show that the soil density becomes negligible when $D_t/B < 2$. For $D_t/B = 1$, the displacement ratio z/D_t exhibits a rapid rise, rocketing from 0 at $T = 0.25$ to approximately 0.8 at $T = 0.45$before reaching unity thereafter. This abrupt collapse can be attributed to the insufficient soil mass above the triggering point as once the arching structure fails; the soil roof becomes too weak to sustain the overburden load. When $D_t/B \geq 2$, the curves are notably smoother and more progressive compared than those observed inloose soil. This results from a stronger soil arch, which delays upward propagation and thereby increases the collapse time.

5.2. Failure mechanism through shear band development

The volumetric strain field for loose and dense soils at different D_t at critical stage are shown in Fig. 12. The results show the differences in strain patterns between loose and dense soils. Loose soil shows a wider and more diffuse strain zone, whereas dense soil exhibits a pronounced localisation pattern. A funnel-like shear region is clearly depicted in loose soil, characterised by gradual lateral widening toward the ground surface. In contrast, a narrower and well-defined region is observed in dense soil. For $D_t/B = 1$, the shear zone forms an almost column-like shape. When increasing D_t/B , the strain area becomes taller and evolves to a parabolic shape. This strain transformation closely mirrors the results of the displacement observed earlier in Fig. 9.

Fig. 13 illustrates the evolution of strain for dense soil with $D_t/B = 3$ across different stages of sinkhole progression. The potential shear bands - narrow zones, where the concentrated deformation leads to failure of ground surface, are highlighted using the red dashed lines. These shapes corroborate with findings from past experimental studies (Dewoolkar et al., 2007; Costa Yuri et al., 2009; da Silva Burke, 2017). At $T = 0.06$, strain primarily concentrates around the cavity roof, and the shear bands form a triangle wedge right above the opening. Additional shear bands developing near the cavity sides can also be observed, showing an inward-growing tendency. At $T = 0.31$, parabolic shear bands emerge and extend upwards, with the upper parts bending inward to form a parabolic shaped zone above the initial triangular region. This indicates the load transfer laterally toward the cavity shoulders, resulting in those parabolic bands. At critical stage ($T = 1$), the initial triangular structure becomes unstable and breaks down as the cavity continues to expand. As a result, the lateral confinement decreases, and the shear zone becomes taller and wider, forming a bigger parabolic profile. This transition

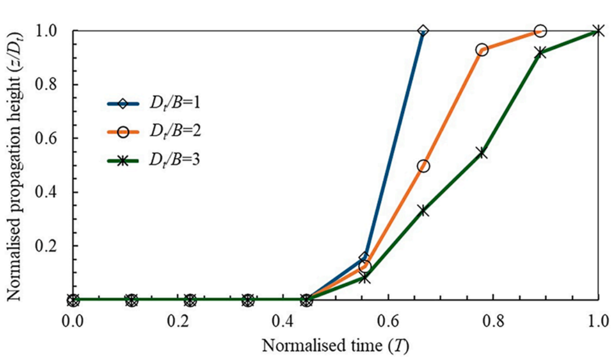

Fig. 10. Influence of different embedment ratio on collapse time of loose soil.

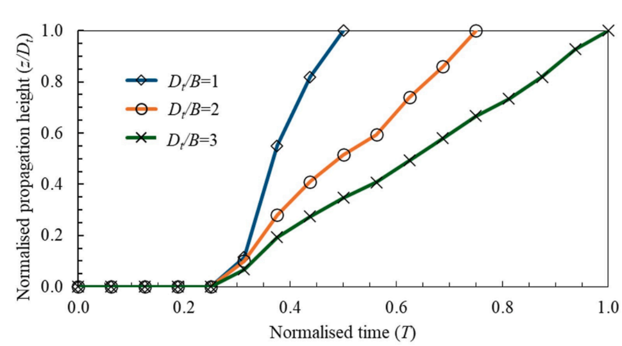

Fig. 11. Influence of different embedment ratio on collapse time of dense soil.

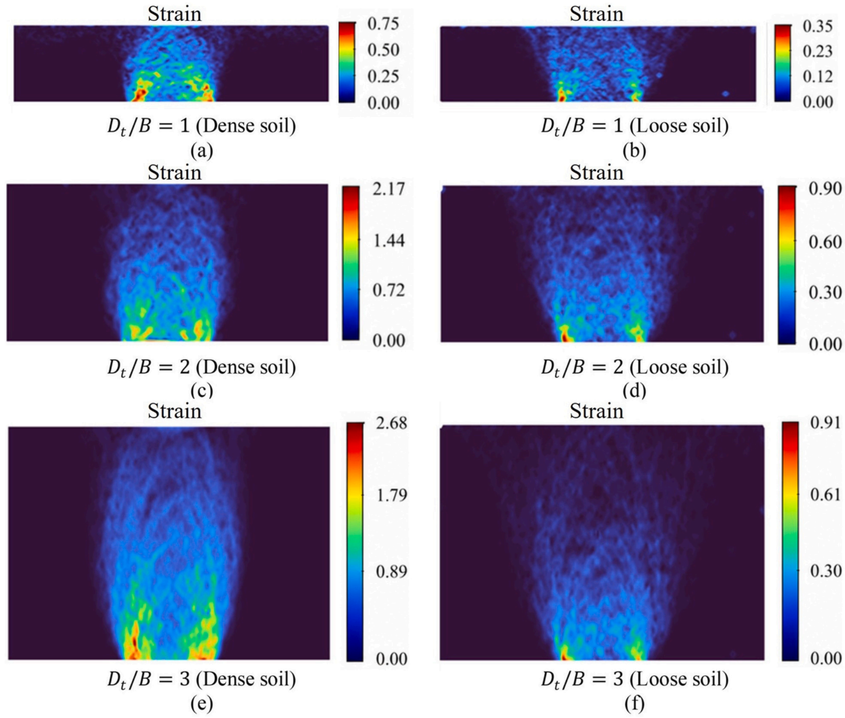

Fig. 12. Strain field at critical stage with different D_t/B for the dense soil case: (a) $D_t/B = 1$, (c) $D_t/B = 2$, (e) $D_t/B = 3$ and for loose soil (b) $D_t/B = 1$, (d) $D_t/B = 2$ and (f) $D_t/B = 3$.

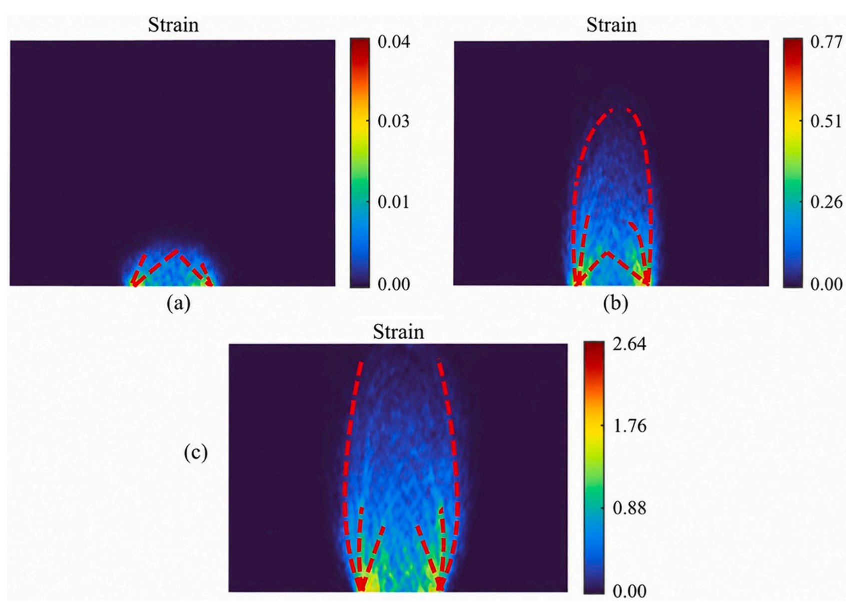

Fig. 13. Shear band evolution patterns at different stages in dense soil: (a) $T = 0.06$, (b) $T = 0.31$ and (c) $T = 1$.

agrees with the shear bands propagation mechanisms of soil identified in previous experimental studies (Behjani et al., 2017; Costa Yuri et al., 2009; Dewoolkar et al., 2007).

5.3. *Influence of particle size scaling on sensitivity of sinkhole collapse mechanism*

Fig. 14 presents the vertical displacement for $D_t/B = 3$ with different particle size scaling ratios, S, ranging from 2 to 4 in loose and dense soils. The results show that particle size scaling shows insignificant influence on the vertical displacement patterns. For loose soil, when S increases, a light difference in the expansion of mobilisation area is observed. Specifically, the displacement shape evolves from a column-like shape at $S = 2$ (Fig. 14a) to funnel-shaped geometry at $S = 4$ (Fig. 14c). This difference can be attributed to the reduced number of particles and lower coordination contact numbers in coarser assemblies, leading to slightly different sample rearrangements and lateral spreading of displacement in loose case. Meanwhile, dense sand exhibits a consistently localised mobilisation pattern for all particle size scaling. This observation further highlights the limited impact of particle size scaling on the modelling results, thus attesting to the reliability of the results reported in this paper.

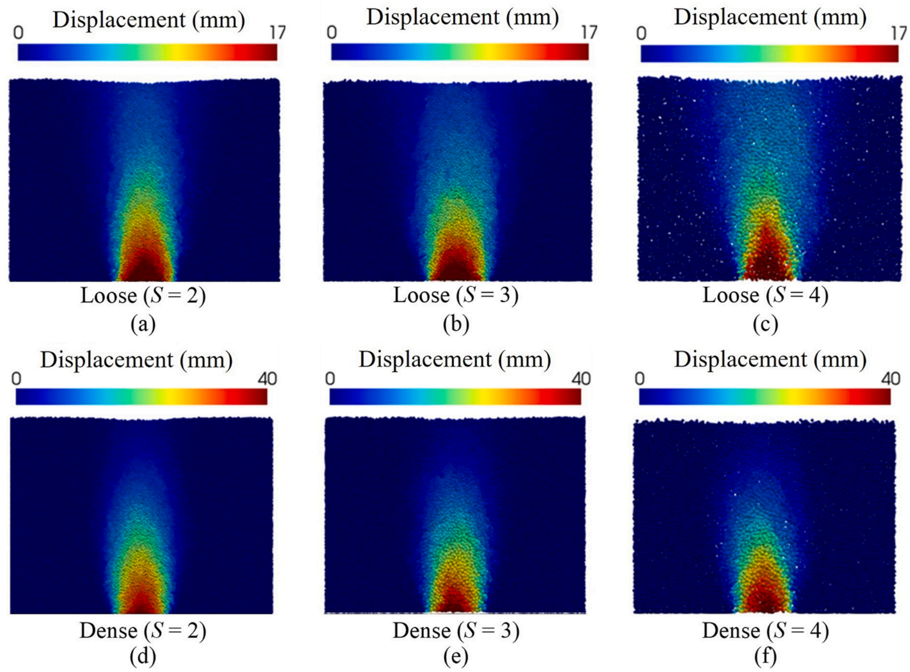

Fig. 14. DEM vertical displacement with different scaling ratio in loose state (a) $S = 2$, (b) $S = 3$, (c) $S = 4$ and dense state (d) $S = 2$, (e) $S = 3$ and (f) $S = 4$ at $D_t/B = 3$.

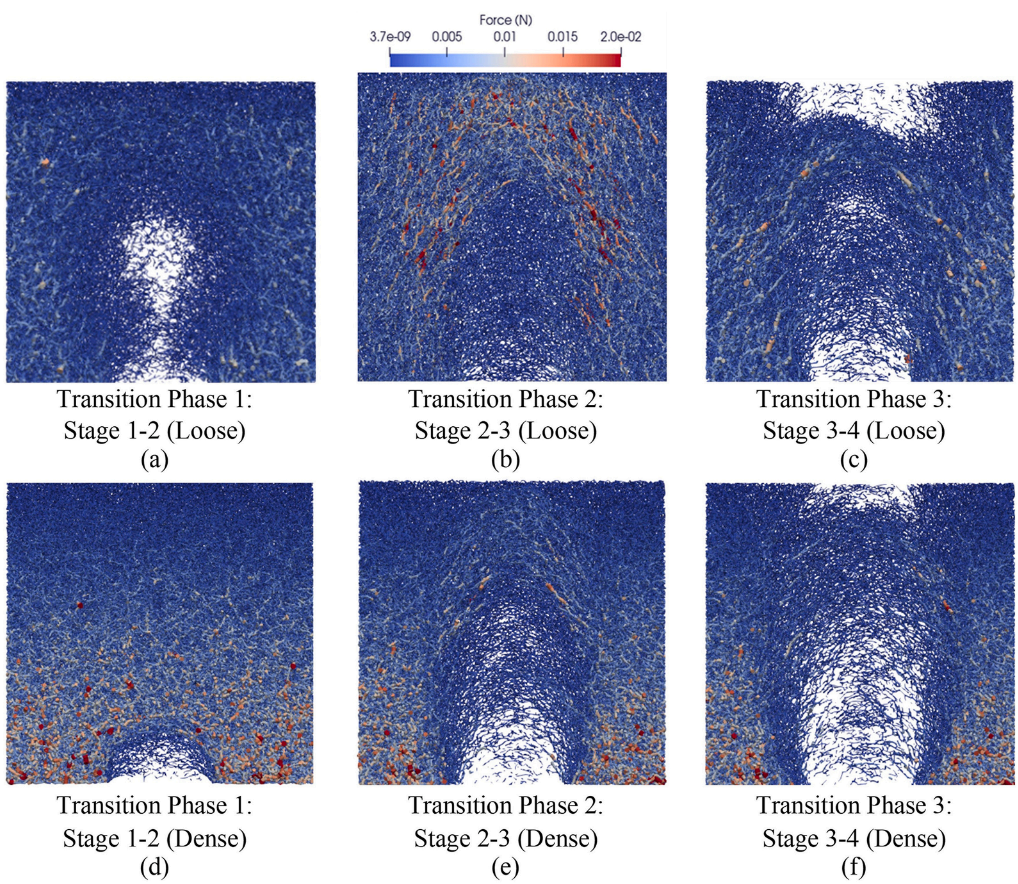

Fig. 15. Contact network in transition phases in: Loose soil (a) Stage 1-2, (b) Stage 2-3, (c) Stage 3-4; and Dense soil (d) Stage 1-2, (e) Stage 2-3 and (f) Stage 3-4 with $D_t/B = 3$.

5.4. Contact network and force evolution

Understanding the evolution of contact networks and force-chain patterns in sinkhole collapse mechanism is particularly essential, as they are the primary factors governing the stress and strain of soil assemblies. Fig. 15 presents the evolution of the contact network during the sinkhole progress for both loose and dense soil states, divided into three distinct phases corresponding to transitions between Stage 1-2, Stage 2-3, and Stage 3-4, as depicted in Figs. 1 and 6. It is worth noting that transition phases are addressed here because they can demonstrate apparent changes in contact network while forming sinkhole. Specifically, transition Phase 1 (Stage 1-2) is the early development associated with the formation of a small arch above the trigging point. Transition Phase 2 (Stage 2-3) shows progressive expansion of void during which a pronounced arch composed of strong contact forces develops to temporarily resist collapse (see Fig. 15b and e). In Phase 2, apparent settlement of ground surface is observed. Transition Phase 3 (Stage 3-4) is the collapse stage, characterised by a marked reduction in contact forces near the crown region, ultimately leading to surface ground collapse. The difference between loose and dense soils can be clearly observed in Phase 1 (Fig. 15a and d). For dense soil, most strong contact forces concentrate at the bottom, reflecting the stronger distribution of overburden stress and tighter packing condition, i.e., stable force-chain arch is also visible directly over the cavity roof. In contrast, the loose soil exhibits a much sparser distribution of strong contact forces and no clearly defined arching structure, indicating a less efficient interparticle load transfer mechanism. In Phase 2, both soils exhibit the appearance of arch structures of contact force. For loose case, an arch-shaped band of elevated forces extending between the two sides of the particle assembly (Fig. 15b), whereas for the dense soil, a more pronounced arch extends from one shoulder to the other, clearly delineating a low-contact region above the cavity (Fig. 15e). These results suggest that the soil experiences continuous “form-and-peel” cycles with repeated process of formation and breakage of successive soil arches. The subsequent arch occurs at a higher location, allowing the cavity to expand upward (Li et al., 2026). At Phase 3, when the void develops to a certain level and a large number of particles lose contact network, force-chain breakage and loss of contact transmission are evident near the surface in both cases, resulting in an upcoming abrupt soil collapse.

To further examine the evolution of contact forces in loose and dense soils, the percentage of strong contacts was quantified relative to the total number of contacts over time, as shown in Fig. 16(a). Strong forces are defined as individual forces whose magnitudes exceed twice the mean force magnitude of the system. In this analysis, the mean force is the average value of all contact forces within the entire simulation domain at a given time step. Forces below this threshold are classified as weak contacts. It is noteworthy that the percentage of strong contacts in loose soil during the collapse stage is indicated by the black dashed line and is not further discussed in this study. Fig. 16(a) indicates the loose soil reaches the critical stage (i.e., the apparent settlement of ground surface due to sinkhole expansion) much earlier than the dense soil, at approximately half of the time in dense case. In early stage, the percentage of strong forces peaks up to 17% soon after the gate removal at $T = 0.15$ (see Fig. 16b), before decreasing and stabilising near the critical stage. This indicates a sudden redistribution of contact forces and rapid rearrangement of the soil skeleton, which is consistent with Phase

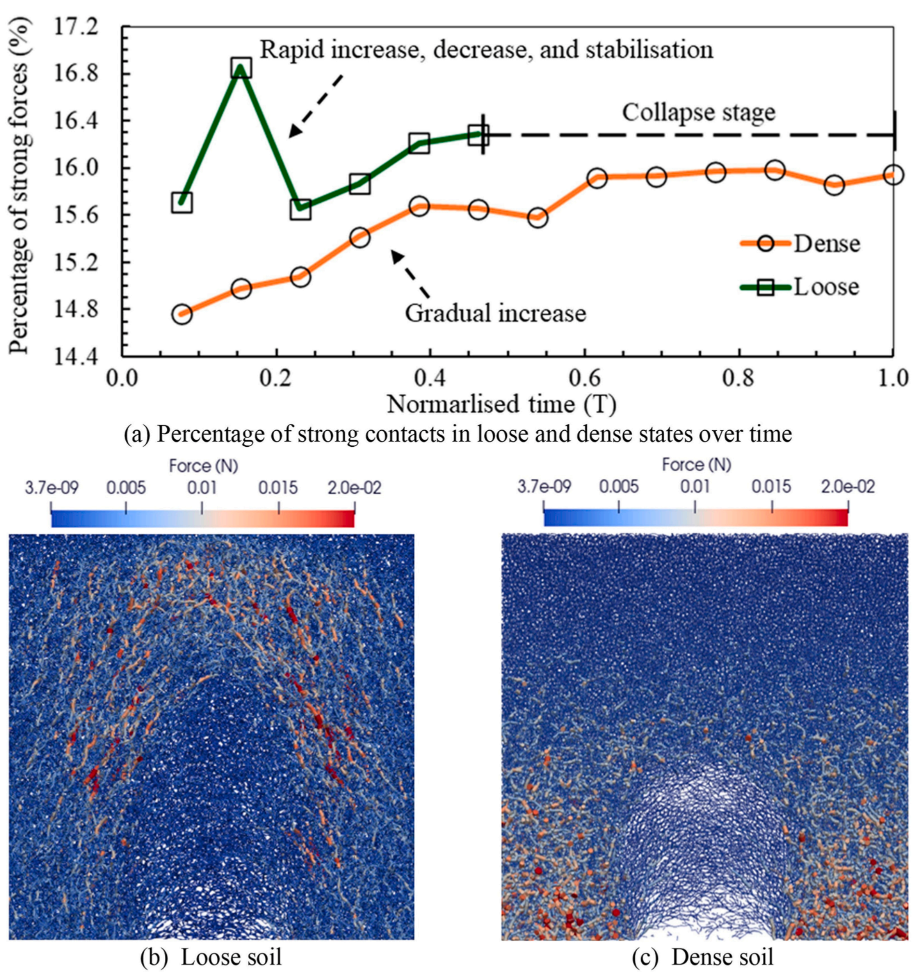

Fig. 16. (a) Percentage of strong contacts in loose and dense states over time; Contact force network at $T = 0.15$ for: (b) loose soil; and (c) dense soil.

2 of the force distribution (Fig. 15b). In contrast, the dense soil shows a more gradual increase in strong forces over time, suggesting progressive mobilisation of force chains and a more stable development of soil arching before collapse.

6. Conclusion

This study combined experimental measurement using Particle Image Velocimetry (PIV) and numerical DEM simulations to investigate the sinkhole development mechanism. Dry sandy soil with different ratios between triggering depth (D_t) and the cavity width B under two distinct compaction states (loose and dense) were examined to characterise the ground collapse through detailed analysis of particulate behaviours. The soil displacement fields obtained from DEM were validated against PIV results. The validated DEM model was then adopted to investigate micro and macroscopic behaviours of soil during sinkhole development. The key conclusions from this work are given as follow:

- The DEM simulations showed consistent agreement with PIV-assisted experiment data in producing vertical displacement fields across different compaction conditions. They confirmed that the magnitude and upward extent of vertical displacement increased with increasing D_t/B in both loose and dense soils. For any given triggering depth, dense soil exhibited highly localised deformation along near-vertical slip surfaces, whereas a laterally broader displacement zone was observed in loose soil.
- Shear bands intersected at middle of the cavity at the beginning, however, overtime, with continued soil loss and progressive failure, additional shear bands appeared, expanding and eventually forming a parabolic profile for dense soil under $D_t/B = 3$. This numerical finding corroborated past theoretical assessments of sinkhole progression.
- The vertical displacement field at critical stage remained closely identical when different particle upscaling factors are used. Specially, varying the particle upscaling factor from 2 to 4 produced only marginal differences in the displacement fields. This finding provides confidence in the reliability of the results analysis presented throughout the paper.
- Three transition stages of force-chain network evolution within 4 major stages of sinkhole development were identified. The most pronounced difference occurred during Transition Phase 1. In Transition Phase 2, soil exhibited repeated cycles of arch formation and collapse as the void grew. In both cases, Transition Phase 3 was marked by fore-chain rupture and a sharp loss of force contacts near ground surface.

Despite these findings, further works are still needed to develop a more comprehensive picture of the sinkhole behaviour. This study focused only on dry soil; therefore, cohesive effects should be incorporated in the future investigations. In addition, the present study adopted a 2D plane-strain model for experimental and PIV analysis, whereas a full 3D model is needed to better capture field-scale sinkhole development. The successful calibration and implementation of the proposed DEM provide a valuable foundation for that extension.

CRediT authorship contribution statement

Tung T. Hoang: Writing – original draft, Visualization, Validation, Software, Investigation, Formal analysis. **Thanh T. Nguyen:** Writing – review & editing, Supervision, Resources, Project administration, Methodology, Funding acquisition, Conceptualization. **Thien Q. Huynh:** Writing – original draft, Resources, Methodology, Investigation, Conceptualization. **Thao Doan:** Writing – review & editing.

Declaration of competing interest

The authors declare that they have no known competing financial interests or personal relationships that could have appeared to influence the work reported in this paper.

Acknowledgements

This study was supported by Australian Research Council (DE230101127) and Transport Research Centre (TRC), University of Technology Sydney.

References

Adrian, R. (1991). Particle-imaging techniques for experimental fluid-mechanics. *Annual Review of Fluid Mechanics, 23*, 261–304. https://doi.org/10.1146/annurev.fluid.23.1.261

Ai, J., Chen, J.-F., Rotter, J. M., & Ooi, J. Y. (2011). Assessment of rolling resistance models in discrete element simulations. *Powder Technology, 206*(3), 269–282. https://doi.org/10.1016/j.powtec.2010.09.030

Al-Halbouni, D., Holohan, E., Taheri, A., Schöpfer, M. P. J., Emam, S., & Dahm, T. (2018). Geomechanical modelling of sinkhole development using distinct elements: Model verification for a single void space and application to the Dead Sea area. *Solid Earth, 9*, 1341–1373. https://doi.org/10.5194/se-9-1341-2018

Al-Halbouni, D., Holohan, E., Taheri, A., Schöpfer, M., Emam, S., & Dahm, T. (2020). *Geomechanical modelling of sinkhole development using distinct elements*. https://doi.org/10.25932/publishup-46843

Al-Naddaf, M., Han, J., Xu, C., Jawad, S., & Abdulrasool, G. (2019). Experimental investigation of soil arching mobilization and degradation under localized surface loading. *Journal of Geotechnical and Geoenvironmental Engineering, 145*(12), Article 04019114. https://doi.org/10.1061/(ASCE)GT.1943-5606.0002190

Augarde, C. E., Lyamin, A. V., & Sloan, S. W. (2003). Prediction of undrained sinkhole collapse. *Journal of Geotechnical and Geoenvironmental Engineering, 129*(3), 197–205.

Behjani, M. A., Rahmanian, N., Fardina bt Abdul Ghani, N., & Hassanpour, A. (2017). An investigation on process of seeded granulation in a continuous drum granulator using DEM. *Advanced Powder Technology, 28*(10), 2456–2464. https://doi.org/10.1016/j.apt.2017.02.011

Burman, B., Kotze, G. P., & Chan, L. (2018). Lane cove tunnel collapse and sinkhole a forensic review - 1: The collapse. *Australian Geomechanics Journal, 53*, 21–32.

Chai, J., Shen, J. S., & Yuan, D.-J. (2018). Mechanism of tunneling-induced cave-in of a busy road in Fukuoka city, Japan. *Underground Space, 3*(2), 140–149. https://doi.org/10.1016/j.undsp.2018.01.003

Coetzee, C. J. (2019). Particle upscaling: Calibration and validation of the discrete element method. *Powder Technology, 344*, 487–503. https://doi.org/10.1016/j.powtec.2018.12.022

Coşkuner, B., İnce, İ., & Barstuğan, M. (2025). Sinkhole detection via deep learning using DEM images. *Natural Hazards, 121*(7), 8347–8366. https://doi.org/10.1007/s11069-025-07127-0

Costa Yuri, D., Zornberg Jorge, G., Bueno Benedito, S., & Costa Carina, L. (2009). Failure mechanisms in sand over a deep active trapdoor. *Journal of Geotechnical and Geoenvironmental Engineering, 135*(11), 1741–1753. https://doi.org/10.1061/(ASCE)GT.1943-5606.0000134

da Silva Burke, T. (2017). *Centrifuge modelling of the behaviour of geosynthetic-reinforced soils above voids.* thesis.

Dave, M., & Juneja, A. (2023). Sinkholes: Trigger, development, and subsidence—A review. In K. Muthukkumaran, R. S. Jakka, C. R. Parthasarathy, & B. Soundara (Eds.), *In proceedings of the soil behavior and characterization of geomaterials* (pp. 289–296). Singapore: Springer Nature Singapore.

Deng, L., Dai, B., Liu, F., Yuan, W., & Yang, J. (2025). Micromechanical exploration of asymmetric mobilization of arching effect in granular materials by DEM. *Particuology, 107*, 176–191. https://doi.org/10.1016/j.partic.2025.10.005

Dewoolkar, M. M., Santichaianant, K., & Ko, H.-Y. (2007). Centrifuge modeling of granular soil response over active circular trapdoors. *Soils and Foundations, 47*(5), 931–945. https://doi.org/10.3208/sandf.47.931

Doan, T., Indraratna, B., Nguyen Thanh, T., & Rujikiatkamjorn, C. (2023). Interactive role of rolling friction and cohesion on the angle of repose through a microscale assessment. *International Journal of Geomechanics, 23*(1), Article 04022250. https://doi.org/10.1061/(ASCE)GM.1943-5622.0002632

Doğan, U., & Yılmaz, M. (2011). Natural and induced sinkholes of the Obruk Plateau and Karapınar-Hotamış Plain, Turkey. *Journal of Asian Earth Sciences, 40*(2), 496–508. https://doi.org/10.1016/j.jseaes.2010.09.014

Duan, Z., Yang, J., Ma, S., & Huang, Z. (2023). Study on instability mechanism of tunnel face in clay-gravel strata under confined water conditions based on DEM-CFD coupling method. *Computers and Geotechnics, 164*, Article 105769. https://doi.org/10.1016/j.compgeo.2023.105769

Elabd, M., Rui, R., Yi, K., He, S.-k., Chen, C., & Ye, Y.-q. (2025). Investigation of soil arching evolution in unreinforced piled embankments with three-dimensional discrete element method-simulated trapdoor tests. *Computers and Geotechnics, 188*, Article 107561. https://doi.org/10.1016/j.compgeo.2025.107561

Eren, Y., Parlar, Ş., Coşkuner, B., & Arslan, Ş. (2024). Geological and morphological features of the karapınar sinkholes (Konya, central Anatolia, Türkiye). *Journal of Earth Science, 35*(5), 1654–1668. https://doi.org/10.1007/s12583-023-1853-z

Fan, L., Zheng, Z., Peng, S., Zhou, J., Shen, T., Wan, H., & Ma, H. (2023). An improved method of active earth pressure on rigid retaining wall under movement modes considering arching effects. *International Journal for Numerical and Analytical Methods in Geomechanics, 47*(3), 410–424. https://doi.org/10.1002/nag.3475

Feng, S.-J., & Wang, Y.-Q. (2025). 3D discrete-element analysis of arching and anchoring within the geogrid-reinforced shallow embankment overlying a void. *Computers and Geotechnics, 186*, Article 107440. https://doi.org/10.1016/j.compgeo.2025.107440

Ferentinou, M. (2020). Sinkhole collapse propagation studies through instrumented small-scale physical models. *Proc. IAHS, 382*, 71–76. https://doi.org/10.5194/piahs-382-71-2020

Fu, P., & Dafalias, Y. F. (2011). Study of anisotropic shear strength of granular materials using DEM simulation. *International Journal for Numerical and Analytical Methods in Geomechanics, 35*(10), 1098–1126. https://doi.org/10.1002/nag.945

Gao, J., Zhu, Y., Jiang, J., Yin, S., Bi, J., & Shen, S. (2025). Analysis of pullout bearing capacity of enlarged head anchors and soil failure modes using discrete element method. *Frontiers in Earth Science, 13*. https://doi.org/10.3389/feart.2025.1564712, 2025.

Garcia Fernando, E., Qian, X., & Bray Jonathan, D. (2025). Discrete element investigation of the role of relative density in soil arching phenomena. *International Journal of Geomechanics, 25*(10), Article 04025230. https://doi.org/10.1061/IJGNAI.GMENG-10811

Ghaayeshthree, S., & Mohd Arif Bin, R. (2025). Study on sinkhole Formation: A comparative analysis of natural Vs human-induced factors. *Progress in Engineering Application and Technology, 6*(2), 74–79.

Gutiérrez, F., Mozafari, M., Carbonel, D., Gómez, R., & Raeisi, E. (2015). Leakage problems in dams built on evaporites. The case of La Loteta Dam (NE Spain), a reservoir in a large karstic depression generated by interstratal salt dissolution. *Engineering Geology, 185*, 139–154. https://doi.org/10.1016/j.enggeo.2014.12.009

Han, J., Bhandari, A., & Wang, F. (2012). DEM analysis of stresses and deformations of geogrid-reinforced embankments over piles. *International Journal of Geomechanics, 12*(4), 340–350. https://doi.org/10.1061/(ASCE)GM.1943-5622.0000050

He, J., Liao, S., Liu, M., Sun, J., & Xi, X. (2023). The soil arching effect induced by shield tunnelling under asymmetric surface loading. *Computers and Geotechnics, 154*, Article 105145. https://doi.org/10.1016/j.compgeo.2022.105145

Huynh, T. Q., Nguyen, T. T., & Indraratna, B. (2025). Evaluating cohesive models in discrete element simulation through drawdown test with new assessment perspectives. *Powder Technology, 452*, Article 120542. https://doi.org/10.1016/j.powtec.2024.120542

Huynh, T. Q., Nguyen, T. T., Indraratna, B., & Doan, T. (2025). Influence of different cohesive contact models on micro-to-macro response of geomaterials: A DEM investigation. *International Journal for Numerical and Analytical Methods in Geomechanics, 49*(16), 3944–3969. https://doi.org/10.1002/nag.70051

Ibrahim, A., & Meguid, M. A. (2023). CFD-DEM simulation of sand erosion into defective gravity pipes under constant groundwater table. *Tunnelling and Underground Space Technology, 131*, Article 104823. https://doi.org/10.1016/j.tust.2022.104823

Indiketiya, S., Jegatheesan, P., Rajeev, P., & Kuwano, R. (2019). The influence of pipe embedment material on sinkhole formation due to erosion around defective sewers. *Transportation Geotechnics, 19*, 110–125. https://doi.org/10.1016/j.trgeo.2019.03.001

Indraratna, B., Nguyen, T. T., Singh, M., Rujikiatkamjorn, C., Carter, J. P., Ni, J., & Truong, M. H. (2021). Cyclic loading response and associated yield criteria for soft railway subgrade – Theoretical and experimental perspectives. *Computers and Geotechnics, 138*, Article 104366. https://doi.org/10.1016/j.compgeo.2021.104366

Iwashita, K., & Oda, M. (1998). Rolling resistance at contacts in simulation of shear band development by DEM. *Journal of Engineering Mechanics, 124*(3), 285–292.

Jacobsz, S. (2015). *Trapdoor experiments studying cavity propagation*.

Jiang, X., Lei, M., & Gao, Y. (2017). Formation mechanism of large sinkhole collapses in laibin, Guangxi, China. *Environmental Earth Sciences, 76*(24), 823. https://doi.org/10.1007/s12665-017-7128-1

Kaufmann, J. (2007). Sinkholes. In *Fact sheet*.

Kaufmann, G. (2014). Geophysical mapping of solution and collapse sinkholes. *Journal of Applied Geophysics, 111*, 271–288. https://doi.org/10.1016/j.jappgeo.2014.10.011

Kobal, M., Bertoncelj, I., Pirotti, F., Dakskobler, I., & Kutnar, L. (2015). Using lidar data to analyse Sinkhole characteristics relevant for understory vegetation under Forest Cover—Case Study of a high karst area in the dinaric Mountains. *PLoS One, 10*(3), Article e0122070. https://doi.org/10.1371/journal.pone.0122070

Ladd, R. S. (1978). Preparing test specimens using undercompaction. *Geotechnical Testing Journal, 1*(1), 16–23. https://doi.org/10.1520/GTJ10364J

Li, Y., Ma, M., Zhang, D., & He, J. (2026). A CFD-DEM method for simulating the erosion evolution of unsaturated silt induced by leakage through underground pipeline defect. *Engineering Analysis with Boundary Elements, 184*, Article 106628. https://doi.org/10.1016/j.enganabound.2025.106628

Li, L., Qin, A., Jiang, L., & Wang, L. (2023). Simplified mathematical modeling to plane strain consolidation considering unsaturated and saturated conditions for ground with anisotropic permeability. *Computers and Geotechnics, 154*, Article 105150. https://doi.org/10.1016/j.compgeo.2022.105150

Lin, X.-T., Chen, R.-P., Wu, H.-N., & Cheng, H.-Z. (2019). Three-dimensional stress-transfer mechanism and soil arching evolution induced by shield tunneling in sandy ground. *Tunnelling and Underground Space Technology, 93*, Article 103104. https://doi.org/10.1016/j.tust.2019.103104

Liu, X.-Y., Franza, A., & Jimenez, R. (2024). Effects of relative density and dilatancy on stress and deformation arching of sand over an active trapdoor. *Computers and Geotechnics, 173*, Article 106485. https://doi.org/10.1016/j.compgeo.2024.106485

Liu, Q.-W., Wang, H.-L., Chen, R.-P., Yin, Z.-Y., Lin, X.-T., & Wu, H.-N. (2022). Effect of relative density of 2D granular materials on the arching effect through numerical trapdoor tests. *Computers and Geotechnics, 141*, Article 104553. https://doi.org/10.1016/j.compgeo.2021.104553

Lommen, S., Mohajeri, M., Lodewijks, G., & Schott, D. (2019). DEM particle upscaling for large-scale bulk handling equipment and material interaction. *Powder Technology, 352*, 273–282. https://doi.org/10.1016/j.powtec.2019.04.034

Muili, O., & Babaie, H. A. (2025). Sinkhole susceptibility analysis using machine learning for west central Florida. *Applied Computing and Geosciences, 27*, Article 100262. https://doi.org/10.1016/j.acags.2025.100262

Nguyen, T. T., & Indraratna, B. (2020). A coupled CFD-DEM approach to examine the hydraulic critical state of soil under increasing hydraulic gradient. *ASCE International Journal of Geomechanics, 20*(9), 4020138–1:15. https://doi.org/10.1061/(ASCE)GM.1943-5622.0001782

Nguyen, T. T., & Indraratna, B. (2023). Influence of varying water content on permanent deformation of mud-fouled ballast. *Transportation Geotechnics, 38*, Article 100919. https://doi.org/10.1016/j.trgeo.2022.100919

Nguyen, T. T., Indraratna, B., & Leroueil, S. (2022). Localized behaviour of fluidized subgrade soil subjected to cyclic loading. *Canadian Geotechnical Journal, 59*(10), 1844–1849. https://doi.org/10.1139/cgj-2021-0550

Nguyen, B.-P., Nguyen, T. T., Nguyen, T. H. Y., & Tran, T.-D. (2022). Performance of composite PVD-SC column foundation under embankment through plane-strain numerical analysis. *International Journal of Geomechanics, 22*(9), Article 04022155. https://doi.org/10.1061/(ASCE)GM.1943-5622.0002494

Pan, B. (2009). Reliability-guided digital image correlation for image deformation measurement. *Applied Optics, 48*(8), 1535–1542. https://doi.org/10.1364/AO.48.001535

Pan, B., Xie, H., & Wang, Z. (2010). Equivalence of digital image correlation criteria for pattern matching. *Applied Optics, 49*(28), 5501–5509. https://doi.org/10.1364/AO.49.005501

Panjami, K., & Anbazhagan, P. (2025). Underground urban cavities: Consequences and identification through an integrated approach. In K. Premalatha, V. B. Maji, M. Muttharam, & R. G. Robinson (Eds.), *Proceedings of the recent advances in geotechnical engineering* (Vol. 1, pp. 77–89). Singapore: Springer Nature Singapore.

Park, K., Soliman, M., Je Kim, Y., & Hyun Nam, B. (2024). Sinkhole stability chart for geotechnical investigation. *Transportation Geotechnics, 45*, Article 101191. https://doi.org/10.1016/j.trgeo.2024.101191

Perozzi, D., Andrade, J., Kaufmann, R., & Puzrin Alexander, M. (2025). LS-DEM guided analysis of geotechnical tests: Exploring strength anisotropy and stress dependency. *Journal of Geotechnical and Geoenvironmental Engineering, 151*(3), Article 04025001. https://doi.org/10.1061/JGGEFK.GTENG-12975

Qiu, G., & Grabe, J. (2012). Active earth pressure shielding in quay wall constructions: Numerical modeling. *Acta Geotechnica, 7*(4), 343–355. https://doi.org/10.1007/s11440-012-0186-3

Roessler, T., Richter, C., Katterfeld, A., & Will, F. (2019). Development of a standard calibration procedure for the DEM parameters of cohesionless bulk materials – Part I: Solving the problem of ambiguous parameter combinations. *Powder Technology, 343*, 803–812. https://doi.org/10.1016/j.powtec.2018.11.034

Stanier, S. A., Blaber, J., Take, W. A., & White, D. J. (2015). Improved image-based deformation measurement for geotechnical applications. *Canadian Geotechnical Journal, 53*(5), 727–739. https://doi.org/10.1139/cgj-2015-0253

Szmigiel, A., & Tajduś, K. (2025). *A comprehensive review of sinkhole modeling and prediction methods*. Archives of Mining Sciences. https://doi.org/10.24425/ams.2025.154664

Tangjarusritaratorn, T., Miyazaki, Y., Sawamura, Y., Kishida, K., & Kimura, M. (2022). Numerical investigation on arching effect surrounding deep cylindrical shaft during excavation process. *Underground Space, 7*(5), 944–965. https://doi.org/10.1016/j.undsp.2022.01.004

Thornbush, M. (2017). Part 1: Contemporary challenges and current solutions in sinkhole occurrence and mitigation. *Journal of Geology and Geophysics, 6*. https://doi.org/10.4172/2381-8719.1000287

Vennari, C., & Parise, M. (2022). A chronological database about natural and anthropogenic sinkholes in Italy. *Geosciences, 12* [Online].

Waltham, T. (2008). Sinkhole hazard case histories in karst terrains. *Quarterly Journal of Engineering Geology and Hydrogeology, 41*(3), 291–300. https://doi.org/10.1144/1470-9236/07-211

Wang, Z.-Y., Liu, J.-C., Tan, Y., & Long, Y.-Y. (2025). Experimental and numerical investigation on internal erosion induced by infiltration of defective buried pipe. *Bulletin of Engineering Geology and the Environment, 84*(1), 38. https://doi.org/10.1007/s10064-024-04073-2

Whittaker, B. N., & Reddish, D. J. (1989). *Subsidence: Occurrence, prediction and control.* Amsterdam, Netherlands;, Netherlands: Elsevier Science Publishers B.V.

Wu, T., Zhang, T., Gu, C., Wang, J., Cai, Y., Sun, H., & Yuan, Z. (2022). Cyclic behavior of saturated clays in plane strain state. *Journal of Geotechnical and Geoenvironmental Engineering, 148*(1), Article 04021172. https://doi.org/10.1061/(ASCE)GT.1943-5606.0002721

Xiao, X., Gutiérrez, F., & Guerrero, J. (2020). The impact of groundwater drawdown and vacuum pressure on sinkhole development. Physical laboratory models. *Engineering Geology, 279*, Article 105894. https://doi.org/10.1016/j.enggeo.2020.105894

Xu, C., Liang, L., Chen, Q., Luo, W., & Chen, Y. F. (2019). Experimental study of soil arching effect under seepage condition. *Acta Geotechnica, 14*(6), 2031–2044.

Youssef, A. M., Al-Harbi, H. M., Gutiérrez, F., Zabramwi, Y. A., Bulkhi, A. B., Zahrani, S. A., Bahamil, A. M., Zahrani, A. J., Otaibi, Z. A., & El-Haddad, B. A. (2016). Natural and human-induced sinkhole hazards in Saudi Arabia: Distribution, investigation, causes and impacts. *Hydrogeology Journal, 24*(3), 625–644. https://doi.org/10.1007/s10040-015-1336-0

Yumba, J., Ferentinou, M., & Grobler, M. (2024). Experimental study of sinkhole propagation induced by a leaking pipe using fibre bragg grating sensors. *Sensors (Basel), 24*(19). https://doi.org/10.3390/s24196215

Zhang, R., Su, D., Lin, X., Lei, G., & Chen, X. (2023). DEM analysis of passive arching in a shallow trapdoor under eccentric loading. *Particuology, 77*, 14–28. https://doi.org/10.1016/j.partic.2022.08.004

Zhao, Y., Shi, Y., Wu, F., Sun, R., & Feng, H. (2021). Characterization of the sinkhole failure mechanism induced by concealed cave: A case study. *Engineering Failure Analysis, 119*, Article 105017. https://doi.org/10.1016/j.engfailanal.2020.105017

Zhou, J., Zhang, L., Zhou, S., & Deng, M. (2023). Investigation of the effect of cyclic loading on the soil arching using damped spring-based trapdoor model. *Computers and Geotechnics, 156*, Article 105279. https://doi.org/10.1016/j.compgeo.2023.105279